



LJMU Research Online

Ran, H, Ma, J, Chen, X, Sun, Y, Gkantou, M and McCrum, D

Local Stability of Laser-Welded Stainless-Steel T-Section Stub Columns

<http://researchonline.ljmu.ac.uk/id/eprint/23329/>

Article

Citation (please note it is advisable to refer to the publisher's version if you intend to cite from this work)

Ran, H, Ma, J, Chen, X, Sun, Y, Gkantou, M and McCrum, D (2024) Local Stability of Laser-Welded Stainless-Steel T-Section Stub Columns. Journal of Structural Engineering, 150 (7). ISSN 0733-9445

LJMU has developed **LJMU Research Online** for users to access the research output of the University more effectively. Copyright © and Moral Rights for the papers on this site are retained by the individual authors and/or other copyright owners. Users may download and/or print one copy of any article(s) in LJMU Research Online to facilitate their private study or for non-commercial research. You may not engage in further distribution of the material or use it for any profit-making activities or any commercial gain.

The version presented here may differ from the published version or from the version of the record. Please see the repository URL above for details on accessing the published version and note that access may require a subscription.

For more information please contact researchonline@ljmu.ac.uk

<http://researchonline.ljmu.ac.uk/>

Local stability of laser-welded stainless steel T-section stub columns

Hongdong Ran ^{a,b}, Jing Ma ^a, Xiangrong Chen ^{a,b}, Yao Sun ^{c,*}, Michaela Gkantou ^d, Daniel McCrum ^e

^a School of Civil Engineering, Xi'an University of Architecture and Technology, Xi'an 710055, China.

^b Key Lab of Structural Engineering and Earthquake Resistance, Ministry of Education (XAUAT), Xi'an 710055, China

^c College of Civil Engineering, Hunan University, Changsha 410082, China.

^d School of Civil Engineering and Built Environment, Liverpool John Moores University, Liverpool L3 3AF, UK.

^e School of Civil Engineering, University College Dublin, Dublin D04 V1W8, Ireland.

* Corresponding author, Email: yaosun@hnu.edu.cn

Abstract: This paper reports an experimental and numerical study on the local stability and compression resistance of laser-welded stainless steel T-section stub columns. An experimental program was first conducted, comprising material coupon tests, residual stress measurements and twenty stub column tests. Upon completion of the laboratory experiments, a numerical modeling program was carried out, where finite-element models were established and validated. The validated finite-element models were then used to perform parametric analyses to derive more numerical data. The obtained numerical and test data were employed to undertake an in-depth design analysis, where the relevant design provisions in the American and European standards as well as the continuous strength method were examined. The design analysis results indicate that the American and European standards lead to significant inaccuracies of the ultimate load predictions, especially for laser-welded stainless steel non-slender T-sections,

26 owing to no consideration of material strain hardening, while the continuous strength method
27 is shown to provide greatly improved design consistency and accuracy over the current
28 American and European standards.

29

30 **Keywords:** Stub column test; Design code; Laser-welded T-section; Stainless steel, Effective
31 width method; Continuous strength method.

32

33 **1. Introduction**

34

35 In recent years, stainless steel has gained extensive utilization in various fields such as bridge
36 and offshore engineering [1–3]. This popularity is attributed to its favorable mechanical
37 attributes, coupled with outstanding durability and resistance to corrosion, resulting in a
38 substantial reduction in the necessity for inspection and maintenance efforts. As an advanced
39 manufacturing method, laser welding has the capability to reduce input heat effectively, thereby
40 resulting in minimal thermal distortions and residual stresses [4]. As a result, the use of laser
41 welding has seen a growing trend in joining stainless steel components to create a diverse range
42 of built-up sections. Research work on laser-welded stainless steel (LWSS) components with
43 different cross-sections and subjected to different loading conditions has been performed, aimed
44 at verifying their structural behavior, examining the applicability of codified design provisions
45 and formulating improved design approaches. Gardner et al. [5] performed laboratory tests on
46 LWSS non-slender I-section stub columns, aimed at investigating their local stability and
47 compressive strengths, while the behavior of their slender counterparts was experimentally

48 examined by Ran et al. [6]. Theofanous et al. [7] and Bu and Gardner [8] performed in-plane
49 bending tests on LWSS angle, channel and I-section beams, aimed at studying their bending
50 behavior. Liang et al. [9,10] experimentally explored the local buckling response of LWSS
51 channels subject to combined loading. The global stability of LWSS angle and I-section
52 columns was examined by Filipović et al. [11], and Gardner et al. [5] through a series of pin-
53 ended column experiments. A testing program was carried out by Bu and Gardner [12] on LWSS
54 beam-columns with non-slender I-sections to explore their structural performance, while the
55 global stability of their slender counterparts was experimentally investigated by Ran et al. [13].
56 This literature review indicated that although comprehensive research on LWSS structural
57 members has been previously conducted, the behavior and strengths of LWSS T-sections
58 remain unexplored; this investigation is thus prompted.

59

60 In this study, a laboratory testing program, comprising material coupon tests, residual stress
61 measurements and twenty stub column tests, was first conducted (Section 2). The
62 experimentally acquired data were analyzed and employed in a numerical modeling program
63 for establishing and validating finite-element (FE) models (Section 3). Based on the completion
64 of validation, the FE models were adopted to carry out systematic parametric studies to generate
65 additional numerical data. On the basis of the acquired numerical and test data, the design
66 provisions in AISC 370 (AISC) [14] and EN 1993-1-4 (EC3) [15] and the continuous strength
67 method (CSM) [16] for LWSS T-sections under compression were evaluated (Section 4).

68

69 **2. Testing program**

70

71 **2.1. Overview**

72

73 A testing program was initially conducted in order to examine the compressive behavior and
74 strengths of LWSS T-sections. Five T-section profiles were adopted in this program, with three
75 different thicknesses considered for each profile, resulting in a total of fifteen T-section sizes,
76 as presented in Table 1. They were manufactured by laser welding from EN 1.4301 austenitic
77 stainless steel sheets, with the welding procedures and techniques satisfying those prescribed
78 in ISO 13919 [17]. The T-sections have been carefully selected to cover both non-slender (Class
79 1–3) and slender (Class 4) cross-sections, according to both the AISC and EC3 cross-section
80 classification frameworks [14,15]. Twenty stub column specimens were fabricated. The
81 geometric sizes of each specimen were measured, involving the specimen length L , the flange
82 width b_f , the section outer height h , the web height h_w and the plate thickness t (see Fig. 1), as
83 presented in Table 1. The overall testing program comprises material tests, residual stress
84 measurements and twenty stub column tests. Detailed descriptions of the key observations and
85 the adopted procedures and setups are provided in the following sub-sections.

86

87

88 **2.2. Material testing**

89

90 Material testing was performed to obtain the material properties of the austenitic stainless steel
91 used. Six material coupons were extracted longitudinally from the three batches of original

92 sheets with the thicknesses of 3 mm, 5 mm and 8 mm, with two coupons for each thickness.
93 Their geometries were in accordance with the specifications of ISO 6892 [18]. The coupons
94 were tested using a 250 kN displacement-controlled universal machine. The test rig is shown
95 in Fig. 2, where an extensometer with a 50 mm gauge length is attached to the central portion
96 of the coupon and two strain gauges are affixed to the coupon. The initial loading rate was set
97 to 0.04 mm/min and subsequently increased to 0.35 mm/min when the 0.2% proof strength was
98 attained. Fig. 3 gives the stress–strain curves obtained from the material testing, while the key
99 material properties, involving the 0.2% and 1.0% proof strengths $\sigma_{0.2}$ and $\sigma_{1.0}$, the ultimate
100 strength σ_u , the Young’s modulus E , the strains respectively at the ultimate stress and fracture
101 ε_u and ε_f , and the R–O parameters n and $m_{1.0}$ [19–21], are averaged and summarized in Table 2.

102

103 **2.3. Residual stress measurements**

104

105 Residual stresses are inevitably introduced into the steel sections during the welding process,
106 which may result in premature failure of the structural members [22]. The residual stresses in
107 the studied LWSS T-sections were therefore measured through the sectioning method. This
108 method has been successfully employed in previous measurements of residual stresses in
109 different welded sections [5,6,23–28]. A total of six sets of residual stress measurements were
110 conducted on T-sections with the T-90×90 profiles, with two repeated measurements for each
111 plate thickness. Fig. 4 shows the locations and dimensions of the strips cut for the residual stress

112 measurements; each strip is nominally 300 mm long and 9 mm wide. Prior to sectioning, two
113 gauge holes with a diameter of 2 mm were drilled along the centerline of the exterior face of
114 each strip and at a distance of 25 mm from the strip ends, through the use of an automatic dot
115 puncher, leading to the nominal length between the gauge holes L_0 equal to 250 mm; the actual
116 strip length between the two gauge holes was thereafter measured using a Demec gauge with
117 250 mm gauge length. Upon length measurements of strips within the T-sections, each specimen
118 was cut into strips, allowing for the release of residual stresses. A typical sectioned T-90×90×3
119 specimen is shown in Fig. 5. The Demec gauge was again adopted for the length measurements
120 of strips between the gauge holes after sectioning. For each strip, the readings of the Demec
121 gauge taken before and after sectioning are respectively denoted as r_1 and r_2 . Hence, the strain
122 ε_{rs} induced by the release of residual stress is calculated as $(r_2-r_1)/L_0$ and the residual stress σ_{rs}
123 can be back-calculated as $E \cdot \varepsilon_{rs}$.

124

125 The six measured sets of residual stresses are presented in a normalized format ($\sigma_{rs}/\sigma_{0.2}$) in Fig.
126 6, which are shown to be in good agreement. Note that there are no codified residual stress
127 predictive models for welded T-sections, whilst the Swedish regulations BSK 99 [29] and
128 European convention ECCS [30] set out predictive models, as shown in Fig. 7 and Table 3. The
129 models are for carbon steel welded I-sections, which can be considered to be geometrically
130 composed of two T-sections. The BSK and ECCS models are plotted in Fig. 6, with their
131 applicability to LWSS T-sections evaluated. It can be seen that the LWSS T-sections contain

132 much lower peak residual stresses than the corresponding predictions from the codified models;
133 this may be attributed to the fact that laser welding can greatly reduce input heat, thereby
134 resulting in lower residual stresses. Moreover, it is observed that the flange tip of T-section has
135 tensile residual stresses, which are contradictory to the compressive residual stress predictions
136 from the codified models. The same finding has been reported in previous studies [23,25,31]
137 on residual stresses in carbon steel welded T-sections. Therefore, the two codified predictive
138 models are proven to be unsuitable for LWSS T-sections. A new predictive model is proposed
139 herein, as defined in Fig. 8 and Table 4, revealing an excellent agreement with the measured
140 residual stress data points.

141

142 ***2.4. Stub column tests***

143

144 For the purpose of investigating the local stability and strengths of LWSS T-sections under
145 compression, stub column tests were conducted on the twenty T-section specimens. All the stub
146 column specimens were tested in a universal machine, which applied concentric compression
147 forces to the specimen ends. It is worth noting that the nominal stub column length was selected
148 in accordance with the recommendations given in Ziemian [32], and set to be equal to three
149 times the outer section height herein; the selected specimen lengths are short enough to prevent
150 the occurrence of member global buckling, but still sufficiently long to incorporate
151 representative residual stress distributions and initial geometric imperfection patterns. Each

152 specimen was initially milled to achieve flat ends and then thoroughly deburred to guarantee a
153 uniform compressive stress distribution on the stub columns during testing. Before testing, the
154 initial local geometric imperfections w_0 of the specimens were measured using a percentage
155 gauge (see Fig. 9), with the measurement procedures in line with those used in previous
156 imperfection measurements [5–10,28,33], and are tabulated in Table 1. Fig. 10 exhibits the main
157 instrumentation adopted in each stub column test, involving four LVDTs and four strain gauges.
158 The strain gauges were affixed to the mid-height faces of the web and flange to measure the
159 corresponding axial strains, while four LVDTs are positioned at the specimen ends to record the
160 end-shortening. Once the test setup was completed, a loading speed of 0.2 mm/min was adopted
161 to drive the universal machine to concentrically compress each test specimen, and all data,
162 comprising the compression loads, the longitudinal strains and the end-shortenings, were
163 simultaneously recorded through using a data acquisition system DATASCAN at an interval of
164 one second. Fig. 11 illustrates the full load versus end-shortening responses for the twenty stub
165 columns, grouped by specimen cross-section profiles, while Table 1 presents the key
166 experimental results, involving the ultimate loads N_u and the corresponding end-shortening δ_u .
167 Finally, the failure modes of five representative LWSS T-section stub column specimens are
168 displayed in Fig. 12, featuring significant local buckling.

169

170 **3. Numerical modeling**

171

172 **3.1. Overview**

173

174 For the purpose of supplementing the laboratory experiments and expanding the acquired data
175 pool, numerical simulations were performed using the ABAQUS FE package [34]. The
176 modeling procedures and techniques used to develop the FE models are first described,
177 followed by a detailed description of a validation study, which compared the established FE
178 model data to the test results. Upon validation, the FE models were adopted and used to perform
179 parametric analyses over a broader range of cross-sectional sizes and aspect ratios.

180

181 **3.2. Establishment and validation of FE models**

182

183 As provided in the ABAQUS element library [34], the ‘S4R’ shell element has been used for
184 simulating a variety of stainless steel members [6,8–10,12,13,24] and was used herein. Through
185 a prior mesh sensitivity investigation, the element size was selected as t . This size was found to
186 (i) enable accurate modeling of residual stresses and (ii) result in proper computational
187 efficiency and accuracy. The engineering material response, acquired from the material testing,
188 was transformed to the true response [6,8] and afterwards used in the FE modeling. Since the
189 performance of thin-walled steel components may be affected by residual stresses, they were
190 incorporated into the FE models utilizing the ‘INITIAL CONDITION’ command [34], with
191 their amplitudes and patterns acquired from the predictive model shown in Fig. 8. Fig. 13
192 illustrates the residual stresses included in the modeled specimen T-60×60×3.

193

194 The fixed-ended boundary conditions were precisely represented in the FE models using
195 constraints. Each end section was coupled to one concentric reference point. The bottom
196 reference point was restrained with no degree of freedom allowed, whilst its top counterpart
197 has longitudinal translation only – see Fig. 13. Incorporation of initial local geometric
198 imperfections was also completed for each stub column FE model. Specifically, an elastic
199 eigenvalue analysis [34] was initially performed for acquiring the lowest local buckling mode
200 of each FE model, which was adopted as the imperfection profile and factored by the
201 corresponding measured imperfection amplitude, according to Table 1.

202

203 Once the FE models were built, the nonlinear analysis ‘Static, Riks’ [34] was used to acquire
204 the numerical response, comprising numerical failure modes and loads as well as load–end-
205 shortening histories. The accuracy of the numerical results from the FE models was examined
206 through comparison with the experimental results. Graphical comparisons between the
207 numerical and test load–deformation histories for the twenty tested stub columns are displayed
208 in Fig. 11, in which the experimental responses are found to be precisely captured by their FE
209 counterparts. The effect of residual stresses on the local stability of LWSS T-sections was also
210 evaluated by comparing the FE load–deformation histories with and without residual stresses,
211 with the results shown in Fig. 14. It can be seen from the figure that the FE load–deformation
212 histories with residual stresses almost coincide with their counterparts without residual stresses,
213 indicating the insignificant effect of residual stresses [9,10]. The mean test-to-FE ultimate load
214 ratio is equal to 1.01, demonstrating that the developed FE models can provide very good
215 predictions of the ultimate loads. In addition to the good agreements between the numerical and

216 test load–deformation histories and ultimate loads, the experimental failure modes were also
217 accurately simulated by the FE models, as depicted in Fig. 15 for two typical specimens.
218 Overall, the established FE models were shown to simulate well the performance of LWSS T-
219 sections under compression and therefore demonstrated to be validated.

220

221 ***3.3. Parametric analyses***

222

223 Upon validation of the FE models, systematic parametric analyses were conducted, aimed at
224 expanding the data bank over a broader spectrum of cross-sectional sizes and aspect ratios,
225 beyond those examined in the testing program. For the modeled T-sections, their geometric
226 dimensions were selected carefully to ensure that all cross-section classes are covered,
227 accounting for both the AISC and EC3 cross-section classification frameworks [14,15].
228 Specifically, the web heights and flange widths ranged from 60 and 200 mm and the thicknesses
229 from 3 to 12 mm, enabling an extensive spectrum of cross-sectional geometries to be examined.
230 All modeled stub columns were developed using the aforementioned modeling techniques,
231 procedures as well as assumptions. In total, numerical data for 169 LWSS T-section stub
232 columns were acquired through parametric analyses.

233

234 **4. Design analysis**

235

236 ***4.1. Overview***

237

238 Based on the laboratory experiments and numerical simulations, a comprehensive design
239 analysis is conducted in this section. The design provisions prescribed in AISC 370 [14] and
240 EN 1993-1-4 [15] for LWSS T-sections under compression are first described, and their
241 suitability is assessed using the numerical and experimental data. The conservatism of the AISC
242 370 and EN 1993-1-4 design provisions is revealed and discussed. The CSM [16], as an
243 alternative design method, is then evaluated, with design prediction improvement observed.
244 The quantitative assessments of the three design methods [14–16] are presented in Table 5,
245 where the mean FE/test-to-predicted ultimate load ratios $N_u/N_{u,pred}$, and their COVs are reported.
246 Figs 16–20 give the graphical assessment results on the basis of the numerical and test data.

247

248

249 **4.2. AISC 370**

250

251 AISC 370 [14] is a recently developed American specification in for stainless steel structures.
252 For T-sections under compression, two section classes are set out in AISC 370 [14], including
253 non-slender T-sections and slender T-sections. The classification of T-sections is conducted by
254 comparing the width-to-thickness ratio of the most slender plate element $\lambda_{max,AISC}$ with the
255 codified limiting width-to-thickness ratio of $\lambda_r=0.41(E/\sigma_{0.2})^{0.5}$. For non-slender T-sections, their
256 compression resistance is defined as the cross-sectional yield load $N_y=A\sigma_{0.2}$. Slender T-sections
257 are susceptible to local buckling that reduces the effectiveness of the full cross-section. To allow
258 for the local buckling effect, the effective width approach is adopted in AISC 370 [14].

259 Specifically, a reduction factor ρ_{AISC} is introduced to reduce the original plate width to the
 260 effective plate width, as defined by Eq. (1), where f_{el} is the elastic local buckling stress of the
 261 cross-section, as calculated from Eq. (2), where ν is the Poisson's ratio and equal to 0.3 for
 262 stainless steel, and λ is the width-to-thickness ratio and equal to $\lambda_{w,AISC}=(h_w+t)/t$ for web and
 263 $\lambda_{f,AISC}=0.5b_f/t$ for flange. A worked example is presented in Appendix A to further demonstrate
 264 the calculation procedures of AISC 370 [14].

$$265 \quad \rho_{AISC} = 0.772 \left(1 - 0.10 \sqrt{\frac{f_{el}}{\sigma_{0.2}}} \right) \sqrt{\frac{f_{el}}{\sigma_{0.2}}} \quad (1)$$

$$266 \quad f_{el} = \frac{0.425\pi^2 E}{12(1-\nu^2)\lambda^2} \quad (2)$$

267

268 Based on the FE and test results, the suitability of the AISC design provisions for LWSS T-
 269 sections under compression is assessed. The numerically and experimentally obtained ultimate
 270 loads N_u are normalized by the section yield loads N_y and plotted against the width-to-thickness
 271 ratio of the most slender plate element $\lambda_{max,AISC}$ (taken as the greater value of $\lambda_{w,AISC}$ and $\lambda_{f,AISC}$)
 272 in Fig. 16. It can be seen from the figure that the current AISC limiting web-to-thickness ratio
 273 λ_r is conservative when used for classifying LWSS non-slender and slender T-sections. A new
 274 limiting ratio $\lambda_{r,p}=0.41(E/\sigma_{0.2})^{0.5}$ is then proposed to improve the accuracy of cross-section
 275 classification, as also depicted in Fig. 16. Regarding the accuracy of the AISC design
 276 compressive resistance $N_{u,AISC}$, a quantitative assessment is undertaken, with the results,
 277 involving the mean ultimate load ratios $N_u/N_{u,AISC}$ and the COVs, given in Table 5(a). The results
 278 show an under-estimation of the mean capacity ($N_u/N_{u,AISC}=1.20$) and considerable
 279 inconsistency, especially for non-slender T-sections (COV=0.067). The conservatism is also

280 observed in Fig. 17, where the load ratios $N_u/N_{u,AISC}$ are plotted against the width-to-thickness
281 ratio of the most slender plate element $\lambda_{max,AISC}$. The graphical assessment evidently
282 demonstrates that the American specification yields rather scattered and conservative strength
283 predictions for LWSS T-sections under compression, due to the ignorance of material strain
284 hardening.

285

286 **4.3. EN 1993-1-4**

287

288 EN 1993-1-4 [15] is a European code established specifically for stainless steel structures.
289 Similar to its American counterpart AISC 370, the Eurocode also adopts the cross-section
290 classification framework, which categorizes cross-sections in compression into non-slender
291 (Class 1–3) and slender (Class 4) sections. For a T-section under compression, its class is
292 determined by comparing the slenderness of its most slender element $\lambda_{max,EC3}$ (taken as the
293 greater value of $\lambda_{w,EC3}=h_w/t$ and $\lambda_{f,EC3}=0.5(b_f-t)/t$) against the Class 3 slenderness limit
294 $\lambda_s=11.5 \cdot (235/\sigma_{0.2})^{0.5}$. The Class 3 slenderness limit is graphically evaluated in Fig. 18 based on
295 the test and FE results for LWSS T-sections, showing high accuracy. Upon completion of the
296 cross-section classification, EN 1993-1-4 [15] prescribes the cross-sectional yield load and
297 effective load as the design resistance $N_{u,EC3}$ for non-slender T-sections and slender T-sections
298 under compression, respectively. The cross-sectional effective load is determined from the
299 effective width approach, as expressed by Eq. (3), in which λ_p is the element slenderness and
300 can be determined from Eq. (4), where λ_1 is equal to $\lambda_{w,EC3}=h_w/t$ for web and $\lambda_{f,EC3}=0.5(b_f-t)/t$
301 for flange. The calculation procedures of EN 1993-1-4 [15] are detailed in a worked example

302 given in Appendix A.

$$303 \quad \rho_{EC3} = \frac{0.655\lambda_p - 0.013}{\lambda_p^2} \quad (3)$$

$$304 \quad \lambda_p = \frac{\lambda_1}{18.2\sqrt{235/\sigma_{0.2}}} \quad (4)$$

305

306 The EC3 design provisions are quantitatively and qualitatively assessed based on the FE and
307 test results. The quantitative assessment results, comprising the mean ultimate load ratio
308 $N_u/N_{u,EC3}$ and COVs, are summarized in Table 5(b), indicating slightly improved design
309 accuracy in comparison with the assessment results of AISC 370 [14]. However, the quantitative
310 assessment also reveals the design conservatism of EN 1993-1-4 [15] for non-slender T-sections
311 under compression ($N_u/N_{u,EC3}=1.23$), which is also found from the qualitative assessment in Fig.
312 19. This may be attributed to that material strain hardening, which is not considered in the
313 design.

314

315 **4.4. CSM**

316

317 The results presented in Sections 4.2 and 4.3 show that the current American and European
318 standards [14,15] lead to conservative strength predictions, especially for LWSS non-slender T-
319 sections, due to the neglect of material strain hardening. To address the inherent conservatism,
320 the CSM [16] that rationally considers strain hardening has been incorporated into the new
321 edition of Eurocode EN 1993-1-4 [14] as an alternative design method. To calculate the CSM
322 cross-section capacity, the first step lies in quantification of the CSM strain limit ε_{csm} that

323 reflects the deformation capacity of the examined T-section under compression; this can be
324 attained by employing the ‘base curve’, expressed by Eq. (5), in which $\varepsilon_y = \sigma_{0.2}/E$ is the elastic
325 strain at the yield strength, $\lambda_{p,cs} = (\sigma_{0.2}/\sigma_{cr,cs})^{0.5}$ is the cross-section slenderness, where $\sigma_{cr,cs}$
326 denotes the elastic local buckling stress of the full T-section under compression and can be
327 identified utilizing the finite-strip package CUFSM [35]. Once the CSM strain limit ε_{csm} is
328 quantified, the CSM cross-section compression capacity $N_{u,csm}$ is determined by utilizing Eq.
329 (6), where E_{sh} is the strain hardening modulus, as given by Eq. (7), in which $\varepsilon_{u,csm} = 1 - \sigma_u/\sigma_{0.2}$ is
330 the CSM ultimate strain. The application of the CSM [16] is demonstrated in detail through a
331 worked example given in Appendix A.

$$332 \quad \frac{\varepsilon_{csm}}{\varepsilon_y} = \begin{cases} \frac{0.25}{\lambda_{p,cs}^{3.6}} \leq \min\left(15, \frac{0.1\varepsilon_u}{\varepsilon_y}\right) & \text{for } \lambda_{p,cs} \leq 0.68 \\ \left(1 - \frac{0.222}{\lambda_{p,cs}^{1.05}}\right) \frac{1}{\lambda_{p,cs}^{1.05}} & \text{for } \lambda_{p,cs} > 0.68 \end{cases} \quad (5)$$

$$333 \quad N_{u,csm} = \begin{cases} A\sigma_{0.2} \frac{\varepsilon_{csm}}{\varepsilon_y} & \text{for } \frac{\varepsilon_{csm}}{\varepsilon_y} \leq 1.0 \\ A\sigma_{0.2} + AE_{sh} \varepsilon_y \left(\frac{\varepsilon_{csm}}{\varepsilon_y} - 1\right) & \text{for } \frac{\varepsilon_{csm}}{\varepsilon_y} > 1.0 \end{cases} \quad (6)$$

$$334 \quad E_{sh} = \frac{\sigma_u - \sigma_{0.2}}{0.16\varepsilon_{u,csm} - \varepsilon_y} \quad (7)$$

335

336 The numerical and test ultimate loads N_u are normalized by the corresponding CSM strengths,
337 $N_{u,csm}$, and plotted against the cross-section slenderness $\lambda_{p,cs}$ in Fig. 20, in which the CSM is
338 shown to be capable of predicting well the FE and test ultimate loads. The graphical evaluation
339 is followed by a quantitative evaluation, with the results given in Table 5(c), where the mean
340 load ratios $N_u/N_{u,csm}$ for non-slender and slender T-sections are equal to 1.08 and 1.04,

341 respectively. The quantitative and graphical evaluations demonstrated that the CSM provides
342 greatly improved design accuracy over AISC 370 and EN 1993-1-4 for LWSS T-sections under
343 compression, due mainly to the rational consideration of strain hardening.

344

345 **5. Conclusions**

346

347 The local stability and load-carrying capacity of LWSS T-sections under compression have been
348 examined through laboratory experiments and numerical simulations. An experimental
349 program, involving twenty stub column tests and supplementary material tests and residual
350 stress measurements, was first conducted. The laboratory experiments were complemented by
351 numerical modeling, with FE models built and validated with reference to the test response.
352 Upon validation, the FE models were utilized in parametric analyses, enabling additional data
353 to be generated over an extensive variety of cross-sectional aspect ratios and dimensions. The
354 numerical data, in combination with the test results, were utilized for assessing the design
355 provisions prescribed in AISC 370 [14] and EN 1993-1-4 [15]. The results show that the
356 codified curves yield conservative predictions of ultimate strength, owing to the neglect of
357 material strain hardening. In particular, on the basis of the experimental and numerical results
358 of this study, $N_u/N_{u,AISC}$ was found to have a mean value of 1.20, while $N_u/N_{u,EC3}$, a mean value
359 of 1.18. The CSM [16] that has been incorporated into the new edition of EN 1993-1-4 as an
360 alternative design method was also examined. The CSM is evidenced to be able to yield more
361 consistent (COV=0.045) and accurate ($N_u/N_{u,csm}=1.06$) ultimate load predictions than its AISC
362 370 and EN 1993-1-4 counterparts.

363

364 **References**

365

366 [1] Baddoo, N. R. (2008). Stainless steel in construction: A review of research, applications,
367 challenges and opportunities. *Journal of Constructional Steel Research*, 64(11), 1199-
368 1206.

369 [2] Gedge, G. (2008). Structural uses of stainless steel—buildings and civil engineering.
370 *Journal of Constructional Steel Research*, 64(11), 1194-1198.

371 [3] Gardner, L. (2019). Stability and design of stainless steel structures—Review and outlook.
372 *Thin-Walled Structures*, 141, 208-216.

373 [4] Ragavendran, M., & Vasudevan, M. (2021). Effect of laser and hybrid laser welding
374 processes on the residual stresses and distortion in AISI type 316L (N) stainless steel
375 weld joints. *Metallurgical and Materials Transactions B*, 52(4), 2582-2603.

376 [5] Gardner, L., Bu, Y., & Theofanous, M. (2016). Laser-welded stainless steel I-sections:
377 Residual stress measurements and column buckling tests. *Engineering Structures*, 127,
378 536-548.

379 [6] Ran, H., Chen, Z., & Ma, Y. (2022). Experimental and numerical studies of laser-welded
380 slender stainless steel I-section columns. *Thin-Walled Structures*, 171, 108832.

381 [7] Theofanous, M., Liew, A., & Gardner, L. (2015). Experimental study of stainless steel
382 angles and channels in bending. *Structures*, 4, 80-90.

383 [8] Bu, Y., & Gardner, L. (2018). Local stability of laser-welded stainless steel I-sections in
384 bending. *Journal of Constructional Steel Research*, 148, 49-64.

- 385 [9] Liang, Y., Zhao, O., Long, Y. L., & Gardner, L. (2019). Stainless steel channel sections
386 under combined compression and minor axis bending–Part 1: Experimental study and
387 numerical modelling. *Journal of Constructional Steel Research*, 152, 154-161.
- 388 [10] Liang, Y., Zhao, O., Long, Y. L., & Gardner, L. (2020). Experimental and numerical
389 studies of laser-welded stainless steel channel sections under combined compression and
390 major axis bending moment. *Thin-Walled Structures*, 157, 107035.
- 391 [11] Filipović, A., Dobrić, J., Buđevac, D., Fric, N., & Baddoo, N. (2021). Experimental study
392 of laser-welded stainless steel angle columns. *Thin-Walled Structures*, 164, 107777.
- 393 [12] Bu, Y., & Gardner, L. (2019). Laser-welded stainless steel I-section beam-columns:
394 Testing, simulation and design. *Engineering Structures*, 179, 23-36.
- 395 [13] Ran, H., Chen, Z., Ma, Y., OBrien, E., & Sun, Y. (2023). Experimental and numerical
396 study of laser-welded stainless steel slender I-section beam-columns. *Engineering*
397 *Structures*, 286, 116128.
- 398 [14] ANSI/AISC 370-21. (2021). Specification for Structural Stainless Steel Buildings,
399 American Institute of Steel Construction (AISC).
- 400 [15] prEN 1993-1-4:2021. (2021). Eurocode 3: Design of steel structures — Part 1-4: General
401 rules – supplementary rules for stainless steels. European Committee for Standardization
402 (CEN), Brussels.
- 403 [16] Gardner, L., Yun, X., & Walport, F. (2023). The continuous strength method–Review and
404 outlook. *Engineering Structures*, 275, 114924.
- 405 [17] ISO 13919-1:2019. (2019). Electron and laser-beam welded joints – Requirements and
406 recommendations on quality levels for imperfections – Part 1: Steel, nickel, titanium and

- 407 their alloys. European Committee for Standardization (CEN), Brussels.
- 408 [18] EN ISO 6892-1: 2016. (2016). Metallic materials: Tensile testing – Part 1: Method of
409 test at room temperature. European Committee for Standardization (CEN), Brussels.
- 410 [19] Ramberg, W., & Osgood, W.R. (1943). Description of stress–strain curves by three
411 parameters. National Advisory Committee for Aeronautics (NACA), Technical note,
412 902, Washington.
- 413 [20] Rasmussen, K. J. (2003). Full-range stress–strain curves for stainless steel alloys. *Journal*
414 *of Constructional Steel Research*, 59(1), 47-61.
- 415 [21] Arrayago, I., Real, E., & Gardner, L. (2015). Description of stress–strain curves for
416 stainless steel alloys. *Materials & Design*, 87, 540-552.
- 417 [22] Li, D., Paradowska, A., Uy, B., Wang, J., & Khan, M. (2020). Residual stresses of box
418 and I-shaped columns fabricated from S960 ultra-high-strength steel. *Journal of*
419 *Constructional Steel Research*, 166, 105904.
- 420 [23] Cao, X., Xu, Y., Kong, Z., Shen, H., & Zhong, W. (2017). Residual stress of 800 MPa
421 high strength steel welded T section: Experimental study. *Journal of Constructional Steel*
422 *Research*, 131, 30-37.
- 423 [24] Sun, Y., Liang, Y., & Zhao, O. (2019). Testing, numerical modelling and design of S690
424 high strength steel welded I-section stub columns. *Journal of Constructional Steel*
425 *Research*, 159, 521-533.
- 426 [25] Liu, J. Z., Chen, S., & Chan, T. M. (2023). Hybrid welded T-section stub columns with
427 Q690 flange and Q355 web: Testing, modelling and design. *Engineering Structures*, 274,
428 115142.

- 429 [26] Yuan, H. X., Wang, Y. Q., Shi, Y. J., & Gardner, L. (2014). Residual stress distributions
430 in welded stainless steel sections. *Thin-Walled Structures*, 79, 38-51.
- 431 [27] Zheng, B., Yang, S., Jin, X., Shu, G., Dong, S., & Jiang, Q. (2020). Test on residual stress
432 distribution of welded S600E high-strength stainless steel sections. *Journal of*
433 *Constructional Steel Research*, 168, 105994.
- 434 [28] Su, A., Sun, Y., Liang, Y., & Zhao, O. (2021). Membrane residual stresses and local
435 buckling of S960 ultra-high strength steel welded I-section stub columns. *Thin-Walled*
436 *Structures*, 161, 107497.
- 437 [29] BSK 99 (1999). Swedish regulations for steel structures. *Boverkets handbok om*
438 *stalkonstruktioner*. Karlskrona, Sweden, 1999.
- 439 [30] ECCS. (1976) European convention for constructional steelwork: convention
440 Europeenne de la construction metallique.
- 441 [31] Xiong, X., Lu, M., & Lu, Y. (2022). Numerical simulation of longitudinal residual stress
442 distribution in welded T-section of Q690 high strength steel. *Journal of Taiyuan*
443 *University of Technology*, 54(1), 107-116. (in Chinese)
- 444 [32] Ziemian, R. D. (2010). Guide to stability design criteria for metal structures. John Wiley
445 & Sons.
- 446 [33] Schafer, B. W., & Peköz, T. (1998). Computational modeling of cold-formed steel:
447 characterizing geometric imperfections and residual stresses. *Journal of Constructional*
448 *Steel Research*, 47(3), 193-210.
- 449 [34] Karlsson Hibbitt, Inc Sorensen, ABAQUS/Standard user's Manual Volumes I-III and
450 ABAQUS CAE Manual. Version 6.14, Pawtucket (USA) 2014.

451 [35] Schafer, B. W., & Adany, S. (2006). Buckling analysis of cold-formed steel members
 452 using CUFSM: conventional and constrained finite strip methods. The 18th International
 453 Specialty Conference on Cold-Formed Steel Structures, Orlando, 39-54.

454

455 **Figures:**

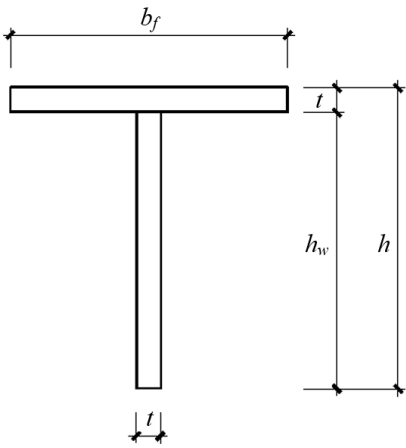


Fig. 1. Notations of LWSS T-section.



Fig. 2. Material test rig.

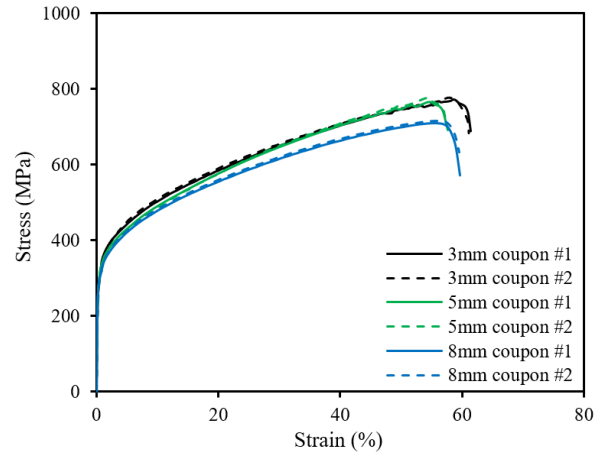


Fig. 3. Measured stress–strain curves.

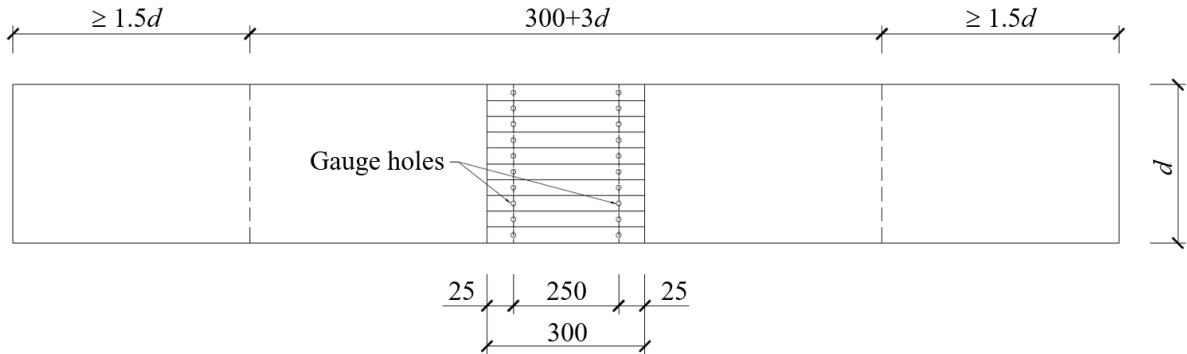


Fig. 4. Illustration of strips cut for residual stress measurements (dimensions in mm).

456

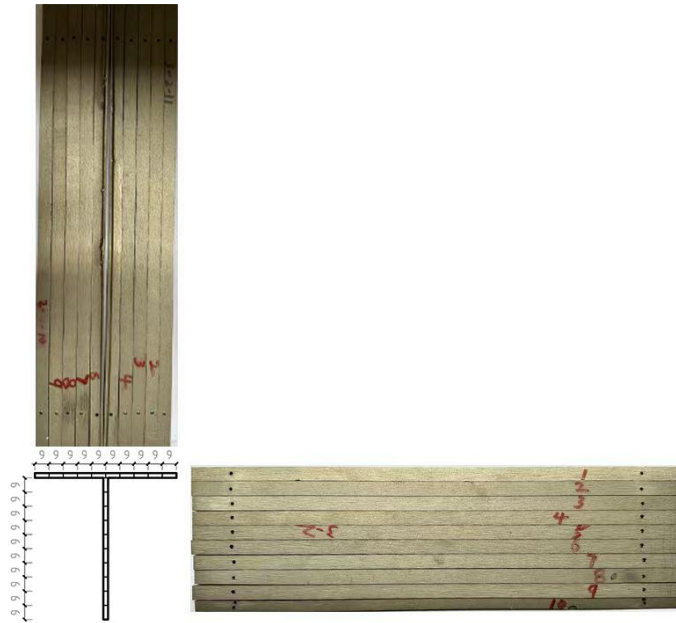
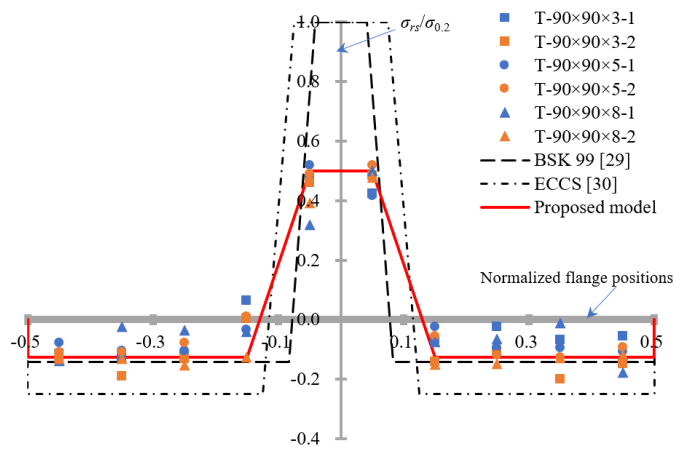
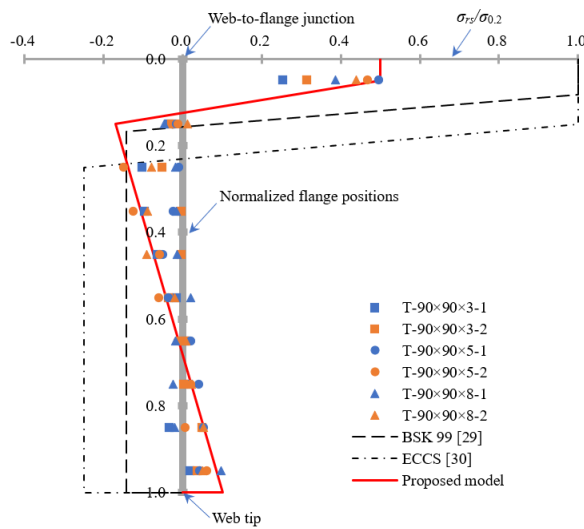


Fig. 5. Sectioned T-90×90×3 specimen.

457



(a) Web.



(b) Flange.

Fig. 6. Comparison of measured residual stresses and predictive models. (Note: Positive and negative values represent tensile and compressive residual stresses, respectively.)

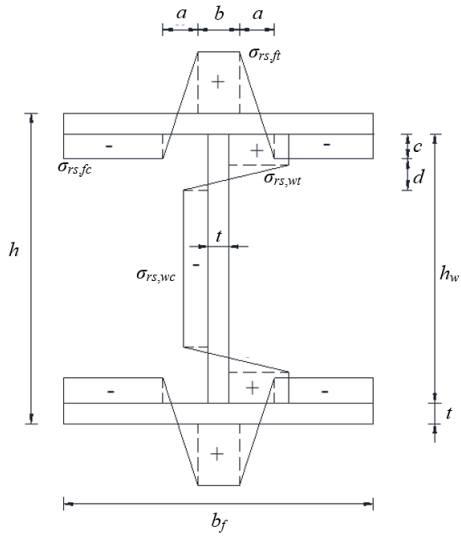


Fig. 7. BSK and ECCS codified residual stress predictive model for I-sections [27,28].

458

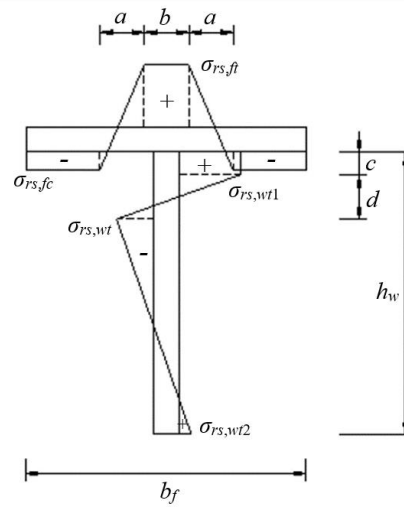


Fig. 8. Proposed predictive model for LWSS T-sections.



Fig. 9. Geometric imperfection measurement rig.

459

460

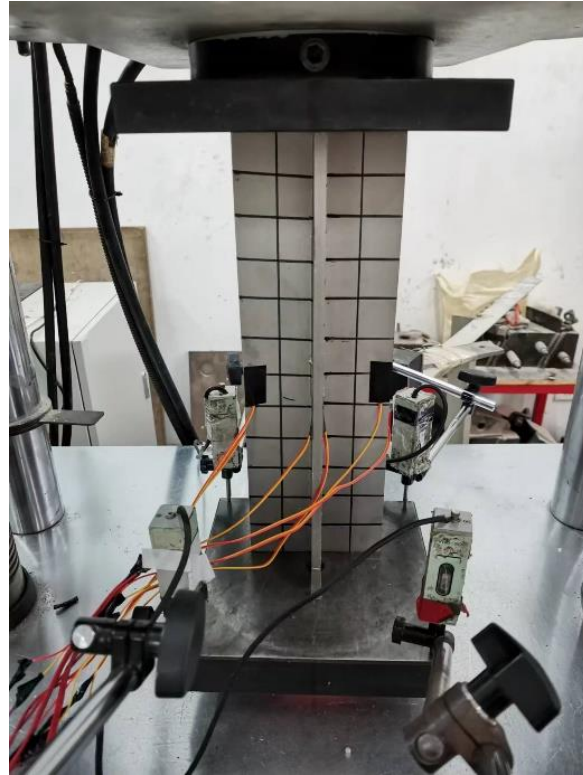
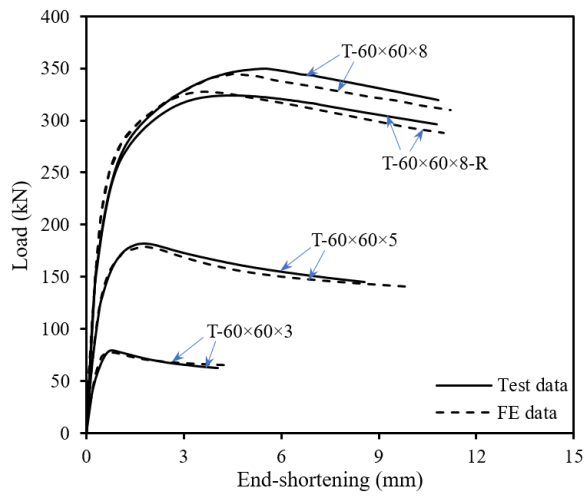
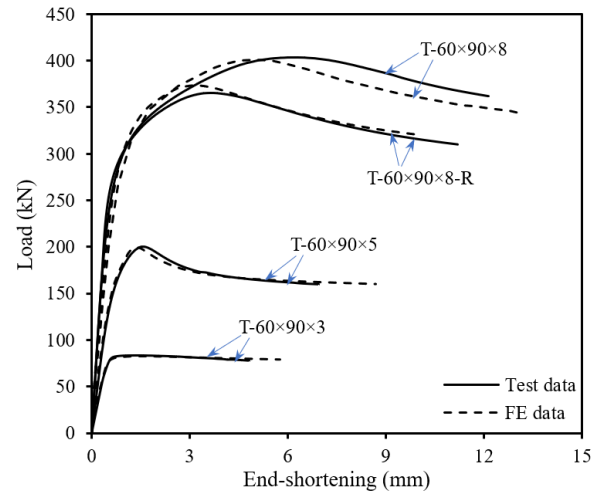


Fig. 10. Stub column test rig.

461



(a) T-60x60 specimens



(b) T-60x90 specimens

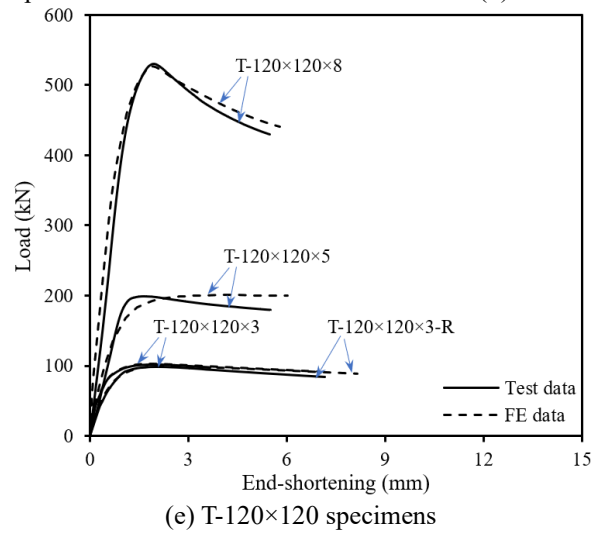
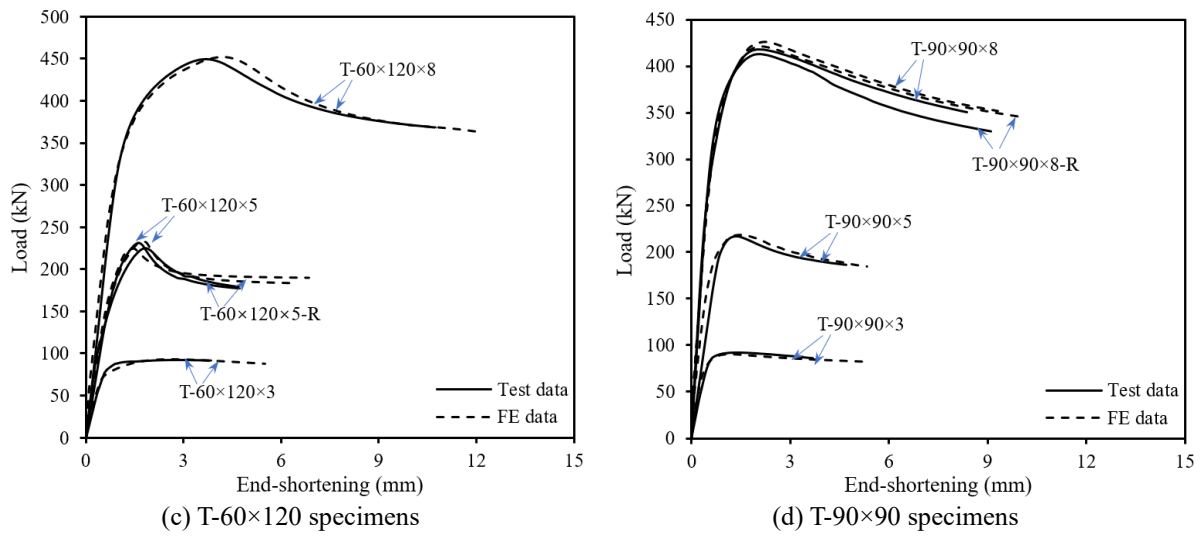


Fig. 11. Test and FE load–end-shortening curves.

462
463
464

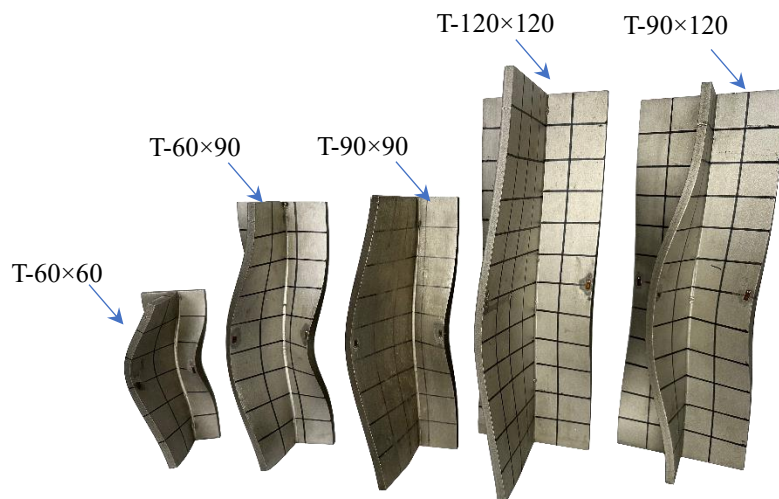


Fig. 12. Failure modes of typical stub column specimens.

465

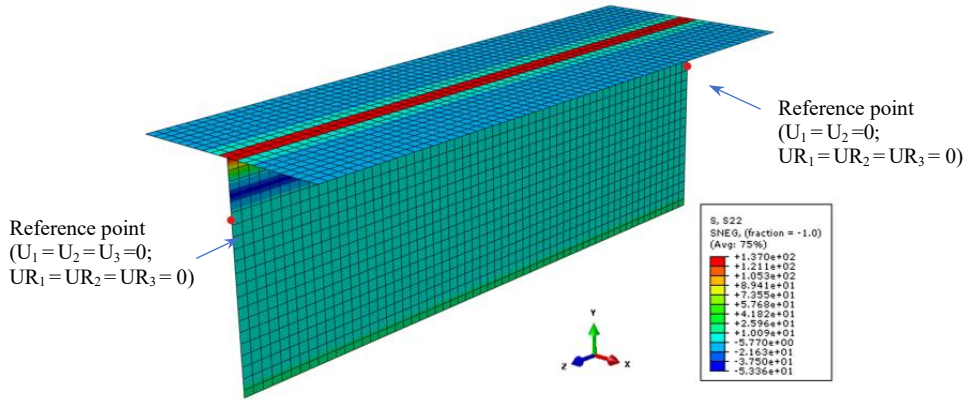


Fig. 13. Residual stresses (in MPa) and boundary conditions for modeled specimen T-60×60×3.

466

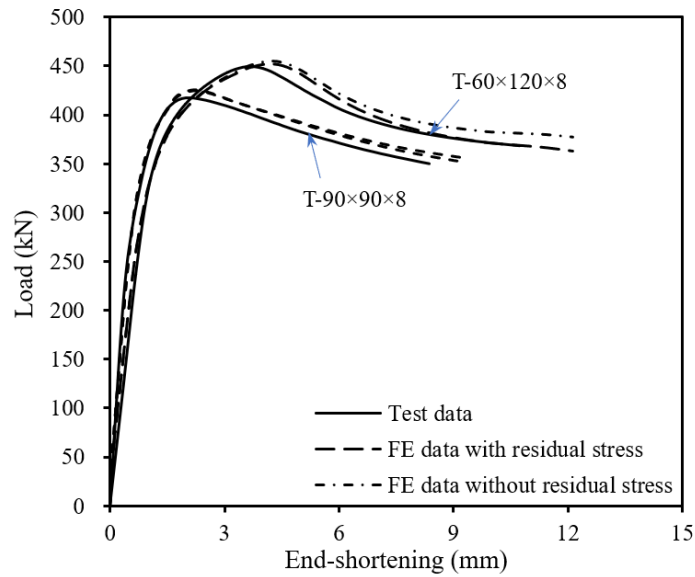


Fig. 14. Evaluation of effect of residual stresses.

467

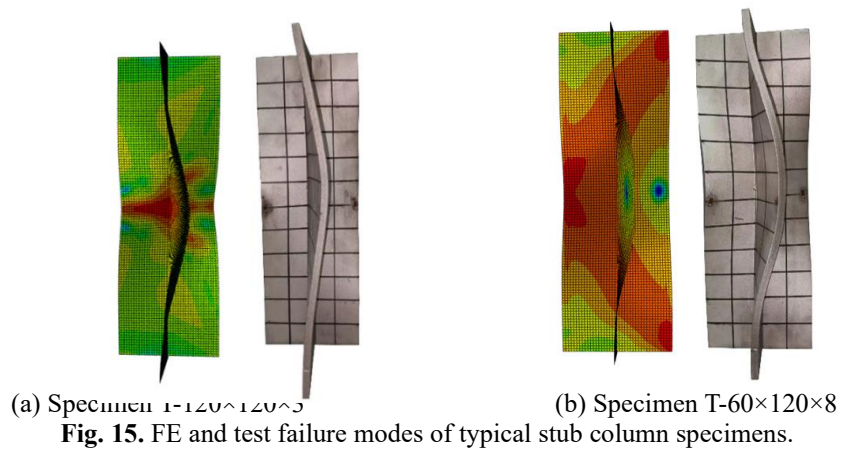


Fig. 15. FE and test failure modes of typical stub column specimens.

468

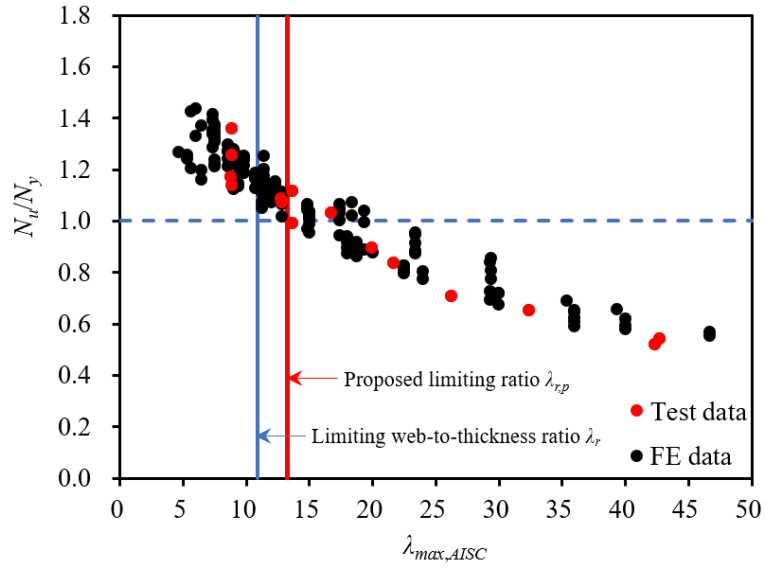


Fig. 16. Assessment of AISC limiting width-to-thickness ratio.

469

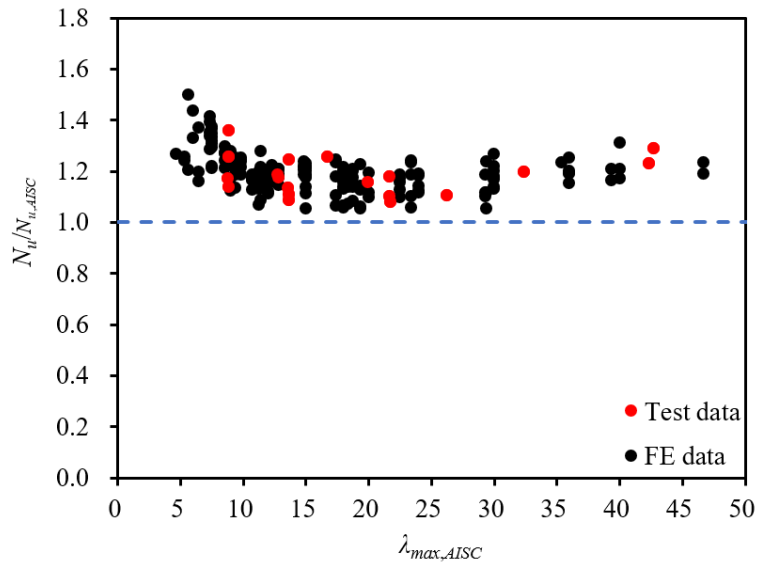


Fig. 17. Comparison of FE/test ultimate loads with AISC predicted ultimate loads.

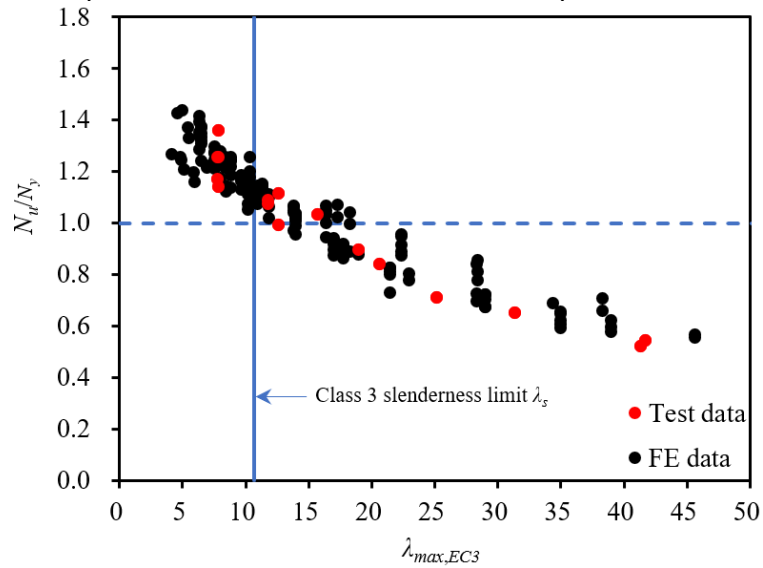


Fig. 18. Assessment of EC3 Class 3 slenderness ratio.

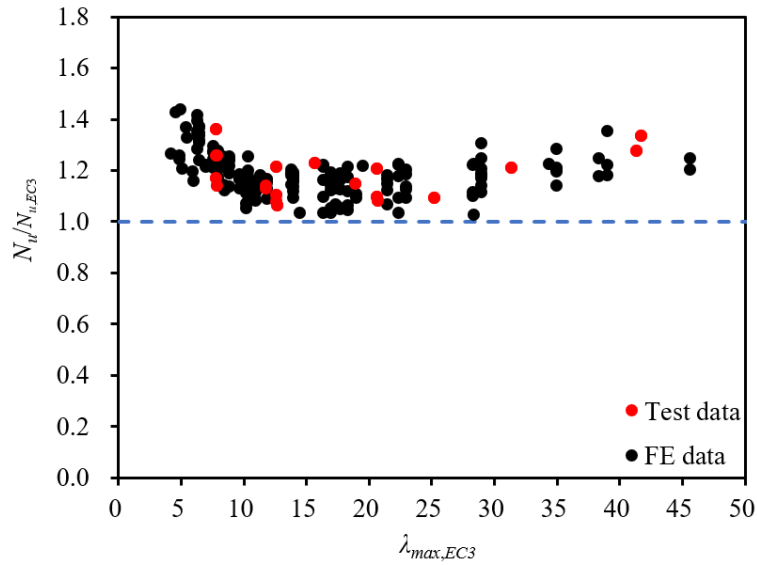


Fig. 19. Comparison of FE/test ultimate loads with EC3 predicted ultimate loads.

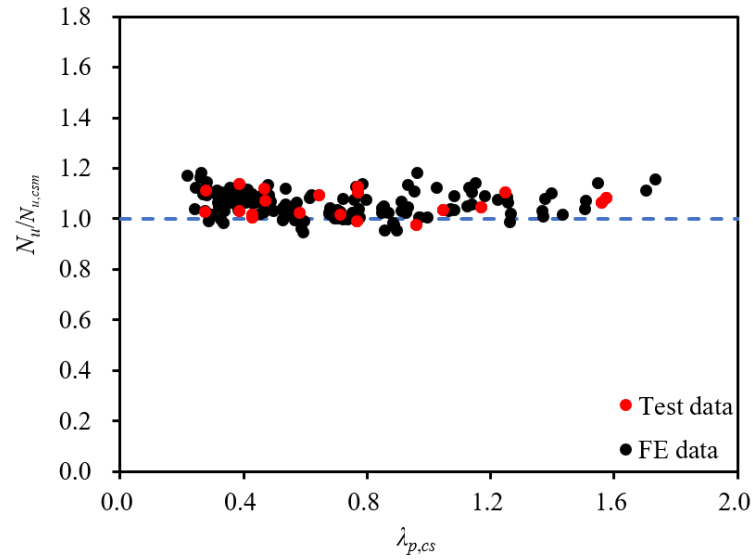


Fig. 20. Comparison of FE/test ultimate loads with CSM predicted ultimate loads.

470 **Tables:**

471

Table 1

Geometric dimensions and test results of stub column specimens.

Specimen	L (mm)	h (mm)	h_w (mm)	b_f (mm)	t (mm)	ω_o (mm)	N_u (kN)	δ_u (mm)
T-60×60×3	179.5	62.4	59.5	59.8	2.89	0.04	79.0	0.76
T-60×60×5	179.4	64.5	59.8	60.9	4.74	0.05	182.1	1.74
T-60×60×8	179.4	67.4	59.8	60.7	7.62	0.09	350.4	5.51
T-60×60×8-R	179.4	67.3	59.7	60.7	7.63	0.05	324.2	4.32
T-60×90×3	269.4	62.5	59.6	89.6	2.89	0.03	83.2	1.35
T-60×90×5	269.5	64.5	59.8	89.6	4.73	0.03	200.5	1.62
T-60×90×8	269.4	67.8	60.2	89.5	7.64	0.10	403.4	5.88
T-60×90×8-R	269.5	67.8	60.2	89.5	7.64	0.04	365.6	3.73
T-60×120×3	359.1	62.7	59.8	119.8	2.89	0.06	92.5	1.01
T-60×120×5	359.5	64.4	59.7	119.9	4.74	0.03	230.9	1.62
T-60×120×5-R	359.5	64.4	59.7	119.8	4.73	0.07	225.5	1.79
T-60×120×8	359.4	67.1	59.5	119.8	7.63	0.11	449.4	3.80
T-90×90×3	269.8	92.7	89.8	89.6	2.87	0.07	91.9	1.02

T-90×90×5	269.9	94.3	89.6	89.6	4.73	0.03	217.2	1.35
T-90×90×8	269.9	97.5	89.9	89.8	7.63	0.06	418.0	1.99
T-90×90×8-R	269.9	97.5	89.9	89.8	7.62	0.03	412.9	2.09
T-120×120×3	359.5	122.7	119.8	119.7	2.88	0.09	102.1	1.25
T-120×120×3-R	359.5	122.7	119.8	119.6	2.90	0.08	98.5	1.38
T-120×120×5	359.9	124.2	119.5	119.5	4.73	0.05	229.1	1.80
T-120×120×8	359.7	127.4	119.8	119.9	7.63	0.06	530.4	2.11

472

473

Table 2

Key measured material properties.

Plate thickness (mm)	E (GPa)	$\sigma_{0.2}$ (MPa)	$\sigma_{1.0}$ (MPa)	σ_u (MPa)	ε_u (%)	ε_f (%)	R–O coefficients	
							n	$m_{1.0}$
3	191.8	274	358	754	54	62	6.3	2.0
5	192.3	286	351	774	53	59	6.8	2.0
8	186.8	281	344	715	53	62	7.6	2.1

474

475

476

477

478

479

480

481

Table 3

Codified residual stress predictive models for carbon steel welded I-sections.

Predictive model	$\sigma_{rs,ft} = \sigma_{rs,wt}$ (tension)	$\sigma_{rs,fc} = \sigma_{rs,wc}$ (compression)	a	b	c	d
BSK 99 [27]	$\sigma_{0.2}$	From equilibrium	$0.75t$	$1.5t$	$1.5t$	$1.5t$
ECCS [28]	$\sigma_{0.2}$	$0.25\sigma_{0.2}$	$0.05b_f$	$0.15b_f$	$0.075h_w$	$0.05h_w$

Note: (i) The subscripts ‘w’ and ‘f’ represent web and flange, respectively.

(ii) The subscripts ‘t’ and ‘c’ represent tension and compression, respectively.

482

483

484

Table 4

Proposed residual stress predictive model for LWSS T-sections.

$\sigma_{rs,ft} = \sigma_{rs,wt1}$ (tension)	$\sigma_{rs,wt2}$ (tension)	$\sigma_{rs,fc} = \sigma_{rs,wc}$ (compression)	a	b	c	d
$0.5\sigma_{0.2}$	$0.1\sigma_{0.2}$	From equilibrium	$0.1b_f$	$0.1b_f$	$0.05h_w$	$0.1h_w$

Table 5

Comparisons of FE/test ultimate loads with predicted ultimate loads.

(a) AISC 370 [14]				
Cross-section	Test data	FE data	$N_u/N_{u,AISC}$	
			Mean	COV
Non-slender	5	51	1.26	0.067
Slender	15	118	1.17	0.048
Overall	20	169	1.20	0.064
(b) EN 1993-1-4 [15]				
Cross-section	Test data	FE data	$N_u/N_{u,EC3}$	

			Mean	COV
Non-slender	5	64	1.23	0.072
Slender	15	105	1.15	0.054
Overall	20	169	1.18	0.070

(c) CSM [16]				
Cross-section	Test data	FE data	$N_u/N_{u,CSM}$	
			Mean	COV
Non-slender	5	64	1.08	0.038
Slender	15	105	1.04	0.043
Overall	20	169	1.06	0.045

487

488

489

490

Appendix – Worked example

491

492 A worked example is presented in this section to demonstrate the calculation procedures of

493 AISC 370, EN 1993-1-4 and the CSM for the design of LWSS T-sections under compression

494 and show the levels of their design accuracy. The calculation is carried out for a typical tested

495 T-section stub column specimen T-120×120×3. The measured cross-section geometric and

496 material properties for this specimen have been reported in Tables 1 and 2 and also presented

497 as follows: $h_w = 119.8$ mm, $b_f = 119.7$ mm, $t = 2.88$ mm, $\sigma_{0.2} = 274$ MPa, $\sigma_u = 754$ MPa and E

498 = 191.8 GPa. The ultimate load is $N_u = 102.1$ kN; the Poisson's ratio $\nu = 0.3$ for stainless steel.

499

500 (I) AISC 370 [14]

501 Step 1: Classification of cross-section

502 The AISC limiting width-to-thickness ratio $\lambda_r = 0.41 \sqrt{\frac{E}{\sigma_{0.2}}} = 0.41 \times \sqrt{\frac{191.8 \times 10^3}{274}} = 10.9$

503 The width-to-thickness ratio of web $\lambda_{w,AISC} = \frac{h_w + t}{t} = \frac{119.8 + 2.88}{2.88} = 42.7 \geq \lambda_r = 10.9$

504 The width-to-thickness ratio of flange $\lambda_{f,AISC} = \frac{0.5b_f}{t} = \frac{0.5 \times 119.7}{2.88} = 20.8 \geq \lambda_r = 10.9$

505 Both the web and the flange are slender plate elements; therefore, the examined T-120×120×3

506 is a slender T-section.

507 Step 2: Determination of effective widths

508 The elastic local buckling stress of the slender web

509
$$f_{el,w} = \frac{0.425\pi^2 E}{12(1-\nu^2)\lambda_{w,AISC}^2} = \frac{0.425\pi^2 \times 191.8 \times 10^3}{12 \times (1-0.3^2) \times 42.7^2} = 40.4$$

510 The reduction factor for the slender web

511
$$\rho_{w,AISC} = 0.772 \left(1 - 0.10 \sqrt{\frac{f_{el}}{\sigma_{0.2}}} \right) \sqrt{\frac{f_{el}}{\sigma_{0.2}}} = 0.772 \left(1 - 0.10 \sqrt{\frac{40.4}{274}} \right) \sqrt{\frac{40.4}{274}} = 0.28$$

512 The effective width of the web $h_{w,eff} = \rho_{w,AISC} h_w = 0.28 \times 119.8 = 33.5$ mm

513 The elastic local buckling stress of the slender flange

514
$$f_{el,f} = \frac{0.425\pi^2 E}{12(1-\nu^2)\lambda_{f,AISC}^2} = \frac{0.425\pi^2 \times 191.8 \times 10^3}{12 \times (1-0.3^2) \times 20.8^2} = 170.6$$

515 The reduction factor for the slender flange

516
$$\rho_{f,AISC} = 0.772 \left(1 - 0.10 \sqrt{\frac{f_{el}}{\sigma_{0.2}}} \right) \sqrt{\frac{f_{el}}{\sigma_{0.2}}} = 0.772 \left(1 - 0.10 \sqrt{\frac{170.6}{274}} \right) \sqrt{\frac{170.6}{274}} = 0.56$$

517 The effective width of the flange $b_{f,eff} = \rho_{f,AISC} b_f = 0.56 \times 119.7 = 67.0$ mm

518 Step 3: Calculation of AISC design compression resistance

519 The AISC effective area of the slender T-section

520
$$A_{eff,AISC} = h_{w,eff} t + b_{f,eff} t = 33.5 \times 2.88 + 67.0 \times 2.88 = 288.6 \text{ mm}^2$$

521 The AISC design compression resistance of the slender T-section

522
$$N_{u,AISC} = A_{eff,AISC} \sigma_{0.2} = 288.6 \times 274 / 1000 = 79.1 \text{ kN}$$

523
$$\frac{N_u}{N_{u,AISC}} = \frac{102.1}{79.1} = 1.30$$

524 **(II) EN 1993-1-4 [15]**

525 Step 1: Classification of cross-section

526 The EC3 Class 3 slenderness limit $\lambda_s = 1.15 \sqrt{\frac{235}{\sigma_{0.2}}} = 11.5 \times \sqrt{\frac{235}{274}} = 10.7$

527 The slenderness of web $\lambda_{w,EC3} = \frac{h_w}{t} = \frac{119.8}{2.88} = 41.7 \geq \lambda_s = 10.7$

528 The slenderness of flange $\lambda_{f,EC3} = \frac{0.5(b_f - t)}{t} = \frac{0.5 \times (119.7 - 2.88)}{2.88} = 20.3 \geq \lambda_s = 10.7$

529 Both the web and the flange are slender plate elements; therefore, the examined T-120×120×3
530 is a Class 4 slender T-section.

531 Step 2: Determination of effective widths

532 The element slenderness of the slender web

533
$$\lambda_{p,w} = \frac{\lambda_{w,EC3}}{18.2 \sqrt{235/\sigma_{0.2}}} = \frac{41.7}{18.2 \times \sqrt{235/274}} = 2.48$$

534 The reduction factor for the slender web

535
$$\rho_{w,EC3} = \frac{0.655\lambda_{p,w} - 0.013}{\lambda_{p,w}^2} = \frac{0.655 \times 2.48 - 0.013}{2.48^2} = 0.26$$

536 The effective width of the web $h_{w,eff} = \rho_{w,EC3} h_w = 0.26 \times 119.8 = 31.1 \text{ mm}$

537 The element slenderness of the slender flange

538
$$\lambda_{p,f} = \frac{\lambda_{f,EC3}}{18.2 \sqrt{235/\sigma_{0.2}}} = \frac{20.3}{18.2 \times \sqrt{235/274}} = 1.21$$

539 The reduction factor for the slender flange

540
$$\rho_{f,EC3} = \frac{0.655\lambda_{p,f} - 0.013}{\lambda_{p,f}^2} = \frac{0.655 \times 1.21 - 0.013}{1.21^2} = 0.54$$

541 The effective width of the flange

542
$$b_{f,eff} = \rho_{f,EC3} (b_f - t) + t = 0.54 \times (119.7 - 2.88) + 2.88 = 66.0 \text{ mm}$$

543 Step 3: Calculation of EC3 design compression resistance

544 The EC3 effective area of the slender T-section

545 $A_{eff,EC3} = h_{w,eff}t + b_{f,eff}t = 31.1 \times 2.88 + 66.0 \times 2.88 = 279.7 \text{ mm}^2$

546 The AISC design compression resistance of the slender T-section

547 $N_{u,EC3} = A_{eff,EC3}\sigma_{0.2} = 279.7 \times 274/1000 = 76.6 \text{ kN}$

548 $\frac{N_u}{N_{u,EC3}} = \frac{102.1}{76.6} = 1.33$

549 **(III) CSM [16]**

550 Step 1: Determination of CSM strain limit

551 The elastic local buckling stress of the T-section is derived using the finite-strip package

552 CUFSM [35] $\sigma_{cr,cs} = 110.2 \text{ MPa}$

553 The cross-section slenderness $\lambda_{p,cs} = \sqrt{\frac{\sigma_{0.2}}{\sigma_{cr,cs}}} = \sqrt{\frac{274}{110.2}} = 1.58$

554 For $\lambda_{p,cs} = 1.58 > 0.68$, $\frac{\epsilon_{csm}}{\epsilon_y} = \left(1 - \frac{0.222}{\lambda_{p,cs}^{1.05}}\right) \frac{1}{\lambda_{p,cs}^{1.05}} = \left(1 - \frac{0.222}{1.58^{1.05}}\right) \frac{1}{1.58^{1.05}} = 0.53$

555 Step 2: Calculation of CSM design compression resistance

556 For $\frac{\epsilon_{csm}}{\epsilon_y} = 0.53 < 1.0$,

557 the CSM design compression resistance of the slender T-section

558 $N_{u,csm} = A\sigma_{0.2} \frac{\epsilon_{csm}}{\epsilon_y} = 688.4 \times 274 \times 0.53/1000 = 100.0 \text{ kN}$

559 $\frac{N_u}{N_{u,csm}} = \frac{102.1}{100} = 1.02$

560

561